The International Journal of Advanced Manufacturing Technology (2019) 102:457–472
https://doi.org/10.1007/s00170-018-3127-y

ORIGINAL ARTICLE

A thermo-mechanical model for simulating the temperature and stress distribution during laser cladding process

Zhe Zhang [1] · Radovan Kovacevic [1]

Received: 2 July 2018 / Accepted: 21 November 2018 / Published online: 4 January 2019

Abstract

During the laser cladding process, thermal stresses are induced because of the high-energy input, high temperature gradient, fast cooling rate, and inconsistency of the clad-substrate material. The induced thermal stresses not only increase the crack tendency, but also influence the mechanical performance of the deposited layer. In this study, a three dimensional (3D) uncoupled thermo-mechanical finite element (FE) model was established to simulate the stress evolution of laser cladding of cobalt-based coatings on mild steel A36. The temperature field was simulated first and then used as transient thermal loading to simulate the stress evolution. Stress distributions for three cases: single track on a flat substrate, double-track on a flat substrate, and double-track on a cylindrical substrate, were investigated in detail. To check the accuracy of the simulation results, validation experiments were carried out using an 8-kW high-power direct diode laser. The thermocouples were used to monitor the temperature cycles at several marked points. The cross-sections of single and double tracks on a flat substrate obtained experimentally were compared with the simulation results. The residual stress on the clad was experimentally determined by an X-ray diffraction machine. The experimentally obtained data showed a significant consistency with the prediction results.

Keywords Laser cladding · Finite element method · Stress evolution

1 Introduction

Laser cladding, an advanced surface modification technique, has attracted extensive and continuous interest from academia and industry for the past 30 years [1]. The major applications of laser cladding include surface protection coatings [2], worn-out component repair [3], and additive manufacturing [4]. Compared to the traditional surface modification methods such as thermal spray and arc deposition, this technology is characterized by several special advantages, namely a low dilution rate, dense clads, metallurgical bond, small distortion, and smaller heat affected zone (HAZ) [5–7].

Though laser cladding has a number of distinct advantages, the process also has several limitations [8]. Among these limitations, cracking is one of the most difficult problems to address. Attributed to laser's rapid heating and cooling nature and inconsistency in the material properties of the deposition material and substrate, high stress is produced both in the cladding layer and HAZ which can easily lead to cracks. As a result, the investigation of the stress evolution of the cladding process can assist researchers and engineers to understand the crack formation and elimination mechanism. However, laser cladding is a very intense metallurgical process. This intensity makes it impossible to monitor the entire thermal and mechanical process just through experimentation [9, 10]. So far, numerical modeling has been proved to be an efficient tool to provide information about the thermal and mechanical fields of the laser cladding process [11–13].

To date, many established numerical models predict the stress field of the laser cladding process. Jendrzejewski et al. [14] investigated the temperature and stress fields induced during laser cladding by FE method. They used temperature independent thermal-mechanical properties in their model. The details of the elastic-plastic model used for simulating the stress were not mentioned. They found that preheating could effectively reduce the stress generated in the clad that consequently lead to the disappearance of micro cracking. Suarez et al. [15] predicted the temperature, strains, and stresses of the laser cladding of Stellite 6 alloy. They used temperature-dependent

✉ Radovan Kovacevic
kovacevi@lyle.smu.edu

[1] Center for laser-aided Manufacturing, Lyle School of Engineering, Southern Methodist University, 3101 Dyer street, Dallas, TX 75206, USA

thermal and mechanical material properties in their model. Suarez et al. assumed that the cladding and substrate materials had an elastoplastic rate-independent model. In detail, they selected the bilinear isotropic model to describe the elastic-plastic behavior of the materials. They reported that the maximum stress existed in the last clad. The lower stresses in the previous tracks were attributed to the stress relaxation produced by the thermal heating of the new clads. Farahmand et al. [16] studied the temperature and stress fields of the high-power direct diode laser cladding process by using the commercial software ANSYS. In their model, the elastic behavior was considered by the Hook's law with the temperature-dependent Young's modulus and Poisson ratio. They combined the bilinear isotropic strain hardening model and von-Mises equivalent stress flow rule to describe the plastic behavior of the material. They observed high von-Mises stress at the clad-substrate bonding zone and the overlapping region of the multi-tracks deposition that identified the locations for crack initiation. Chew et al. [17] investigated the laser cladding–induced residual stress of the single and multi-tracks deposition process. In their model, the effects of the laser-powder interaction on the thermal process and subsequently on the residual field were investigated in detail. They used the Johnson-Cook model to describe the plastic behavior of the material. They also considered the anneal effect during the multi-track deposition in their model. They found tensile stresses in both the coatings of the single and multiple cladding layers. Similar to Suarez's results, Chew et al. observed a relief of stress in the longitudinal and transverse stresses at the initial track during double-track cladding. Bailey et al. [18] modeled the residual stress of multi-track laser deposition of tool steel. Except for the elastic and plastic strains, they considered the strain induced by the phase transformation in their model. The phenomenon that the molten pool did not hold stress was also included in their model. The elements in the molten pool were deactivated to remove their stress. Then, the elements were reactivated during the solidification to initialize the stress to zero. It was found that the phase transformation strain resulted in compressive stress that existed near the surface of the clads. Moreover, the tempering of martensite due to the multi-track heating resulted in variation of compressive stress at the top surface of the deposited layers.

Cobalt-based alloys are used mostly for components exposed to wear, abrasion, and corrosion at moderate and high temperatures. The Co element provides an FCC austenite structure. The Cr in the cobalt-based alloy is responsible mainly for high-temperature oxidation and corrosion resistance, and the material hardening through the solid solution and precipitation of carbides [19]. Other additional elements such as W and Mo also strengthen cobalt-based alloys through solid solution and formation of carbides [20]. As it is known, the components in need of repair and surface protection are usually made of steel. Therefore, the precipitation of carbides, inconsistent physical material properties, and cyclic thermal loading lead to a higher susceptibility of cracks during the laser cladding of cobalt-based materials.

Based on the above reviews, the studies on the stress evolution during the laser cladding process were published extensively. However, most FE models were established on flat workpieces. The study of the residual stress distribution on a cylindrical substrate was not widely published. In this study, a 3D thermo-mechanical coupled FE model was established to study the stress field of the high-power direct diode laser cladding (HPDDL) process. The effect of laser-powder interactions on the thermal results was investigated. The clad geometry used for simulation was directly obtained from the experiment. In order to simulate the clad material deposition, the element birth and death technique was adopted. Two cases, single-track flat model and double-track flat model, were first developed to validate the established models. Then the stress evolutions in the double-track cylindrical model were further investigated in detail. Experiments were executed to validate the accuracy of the proposed model. The thermal cycles of several marked points were monitored by thermocouples. The cross-section micrographs of the cladded layers were also compared with the simulated thermal results. The residual stress on the single- and double-track flat cases was experimentally determined by the X-ray diffraction technique.

2 Experimental setup

Figure 1 shows the experimental setup applied for the laser cladding process. The laser used in the setup was a Coherent direct diode laser with a maximum power of 8 kW and a wavelength of 975 nm. The motion system used was a 6-axis KUKA robot. The molten pool was shielded by inert gas argon (Ar) during deposition to avoid oxidization. The commercial powder Stellite 6 with a size between 53 and 105 μm was selected as the cladding material. The substrate material was A36 mild steel. The temperature evolutions at the

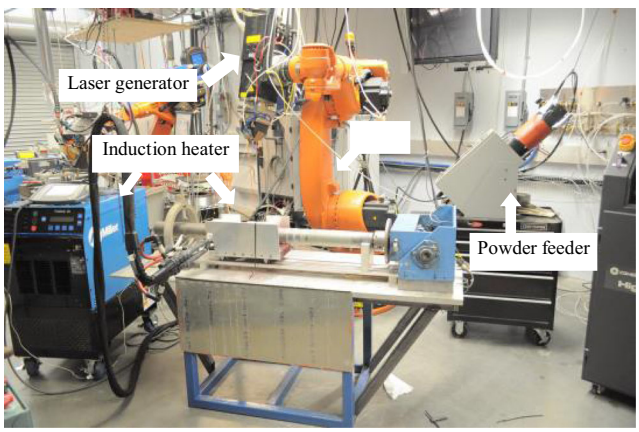

Fig. 1 Experimental setup

HAZ were recorded using chromel-alumel (K-type) thermocouples. The PROTO-LXRD residual stress measurement system was adopted to determine the residual stress experimentally. Before the XRD test, the clad surface was electrochemically polished to remove the un-melted powders. The copper and chromium targets were applied respectively to obtain the residual stress measurement for the cobalt material and the A36 mild steel substrate. The laser cladding parameters used in the current study were as follows: a laser power of 3900 W, scanning speed of 5 mm/s, powder feed rate of 0.62 g/s, and overlapping ratio of 25%. Three investigative cases were designed in this study. Cases 1 and 2 represented the laser cladding of single and double tracks on the flat substrate, whereas Case 3 represented laser cladding of double tracks on the cylindrical substrate. The dimensions of the substrate for Cases 1 and 2 were 30 mm × 50 mm × 9 mm. The inner and outer radii for the cylindrical substrate were 15 mm and 30 mm, respectively.

3 Laser-powder interactions

During the cladding, the powder streams absorbed energy from the laser beam, leading to the increase of power temperature. Meanwhile, the laser power was attenuated by the powder streams due to the shadow effect before it reached the substrate. Therefore, this interaction greatly influenced the energy brought into the substrate, and consequently affected the thermal and stress field distribution. In our previous work [21], the equations used for calculating the laser power attenuation and powder temperature were established. In the current study, only the calculated results were given and the details of the equations and derived procedure could be found in Ref. [21].

Figure 2 shows the laser intensity distribution at the laser focal surface after the attenuation effect. As Fig. 2 illustrates, only 1.43 to 1.76% of the laser power is attenuated. Therefore, the laser power attenuation effect by the feeding powders can be ignored in this study. Figure 3 shows the powder temperature distribution at the focal surface. The maximum powder temperature was found to be at the center of the focal plane with a value of 164.6 °C. The minimum powder temperature was located at the boundary of the focal plane with the value of 60.4 °C. Evidently, the powder was not melted before it came into the molten pool.

4 Finite element model

4.1 Thermal analysis

The transient heat conduction equation was used to describe the heat transfer of the laser cladding process (see Eq. (1)).

$$\frac{\partial}{\partial x}\left(K\frac{\partial T}{\partial x}\right)+\frac{\partial}{\partial y}\left(K\frac{\partial T}{\partial t}\right)+\frac{\partial}{\partial z}\left(K\frac{\partial T}{\partial z}\right)+q_{laser}(x,y,z,t)=\rho C_P\frac{\partial T}{\partial t} \tag{1}$$

where K is the thermal conductivity (W/mK), C_P is the specific heat capacity (J/kg/K), ρ is density (kg/m^3), and q_{laser} represents the intensity of the laser.

Figure 4 shows the laser intensity distribution of the HPDDL beam. The laser intensity presents a top-hat distribution with a rectangular shape. The focused laser beam has a size of 12 mm × 3 mm. The mathematic description of the laser beam intensity is given in Eq. (2).

$$q_{laser}(x,y,z,t)=\begin{cases}\eta\dfrac{P}{w\times L}\left(-\dfrac{6(x-x_c)^2}{d^2}\right) for\ |Y|\le 0.26w\\ \eta\dfrac{P}{w\times L}\left(-\dfrac{6(x-x_c)^2}{d^2}\right)\left(0.3+\dfrac{1-0.3}{0.24w}(0.5w-|Y|)\right) for\quad 0.26w\le|Y|\\ 0\quad for\quad |Y|\ge 0.5w\end{cases} \tag{2}$$

where η, P, w, and L represent the energy absorption rate, laser power, width, and length of the laser spot, respectively.

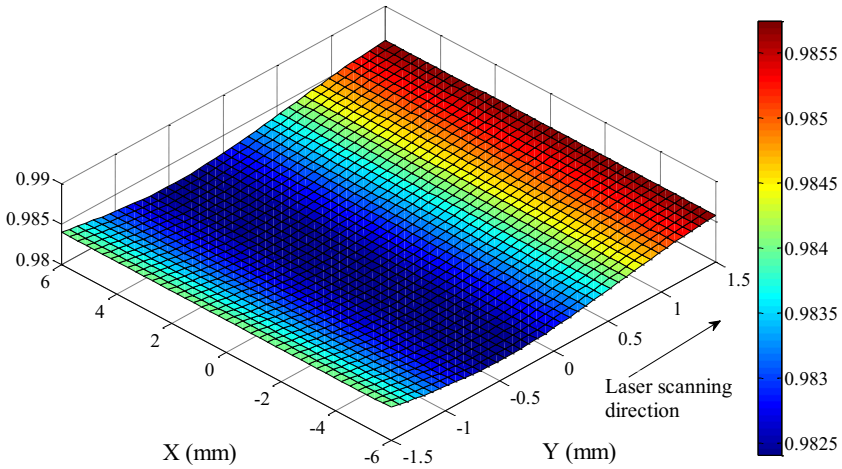

Fig. 2 Laser power attenuation distribution at focal plane

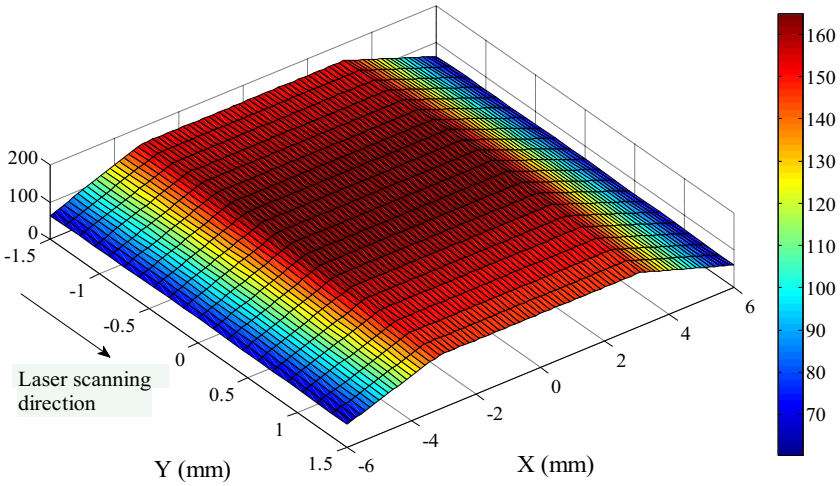

Fig. 3 Powder temperature distribution at focal plane

The heat dissipation on the boundary of the model by the convection and radiation is defined by Eq. (3).

$$-K(T)\frac{\partial(T)}{\partial n} = h_l(T-T_0) \tag{3}$$

where T and T_0 are the temperature at the boundary and the initial temperature, respectively. h_l is the lumped coefficient combining the effects of convection and radiation. The equation for calculating the lumped coefficient is described as [22].

$$h_l = 24.1 \times 10^{-4}\varepsilon T^{1.61} \tag{4}$$

where ε is the emissivity.

Before cladding, a room temperature of 25 °C was assigned both to the substrate and the cladding material.

4.2 Mechanical analysis

A thermal-elastic-plastic model was adopted to simulate the laser cladding stress field. The total strain of the laser cladding process is described by four components (see Eq. (5)).

$$\varepsilon = \varepsilon^e + \varepsilon^p + \varepsilon^t + \varepsilon^{ph} \tag{5}$$

where ε^e is the elastic strain, ε^p is the plastic strain, ε^t is the thermal strain, and ε^{ph} is the phase transformation induced strain. The microstructure of cobalt-based material was characterized by presence of the austenite phase during the laser cladding process. Therefore, the phase transformation induced strain (ε^{ph}) could be ignored during simulation. The isotropic Hooke's rule was used to model the elastic strain. The thermal expansion coefficient was adopted to calculate the thermal strain. The rate-independent kinematic strain hardening model and the von-Mises yield criterion were combined to model the plastic strain [23].

4.3 Material properties and related modifications

The thermal and mechanical material properties were considered as temperature dependent to increase the simulation accuracy. The details of the temperature-dependent material properties

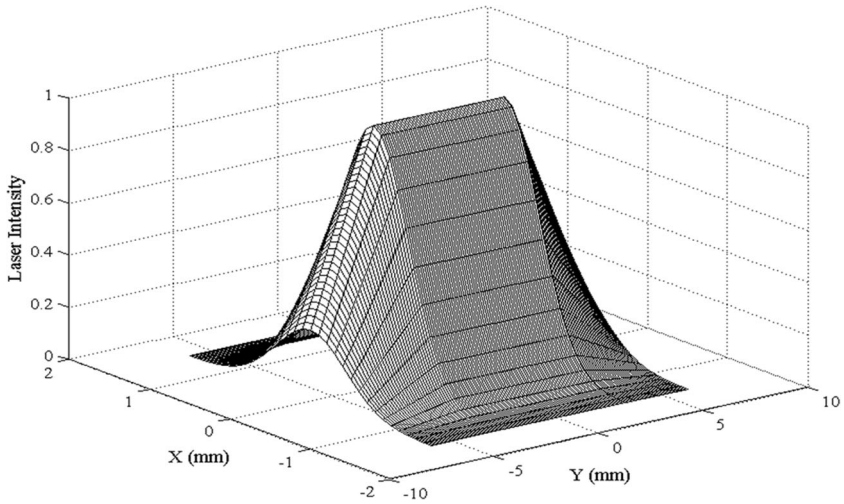

Fig. 4 Schematic view of top-hat power distribution

are plotted in Fig. 5. The thermal conductivity at the temperature above the melting point was modified by multiplying a constant value to compensate for the fluid flow in the molten pool [25]. The latent heat of fusion was involved in the specific heat between the liquid and solid temperature of the materials. The modification equation is described in Eq. (6) [26].

$$C_p^m = \frac{L_f}{T_s - T_l} + C_p(T) \quad T_s \le T \le T_l \tag{6}$$

where L_f represent material's latent heat of fusion, C_p^m is the modified specific heat, $C_p(T)$ is the material's specific heat at temperature T, and T_s and T_l are the solid and liquid temperatures of the material, respectively,

4.4 Geometry and mesh

Figure 6 illustrates the geometry and mesh of the three cases. A gradient mesh was chosen in order to increase the simulation accuracy as well as the calculation efficiency. The laser irradiation region and the HAZ were divided densely whereas the substrate away from the cladding region was meshed sparsely.

4.5 Element birth and death

In order to simulate the additive nature of the laser cladding process, the element birth and death technique in the ANSYS software was used. Before simulation, all built elements in the clad layers were deactivated. During the simulation, the elements were activated when two criteria were satisfied. First criterion is that the elements are irradiated by the laser heat source. Second, the front surface of the molten pool is considered as an ellipsoid shape [16, 27] and only the elements below the ellipsoid surface are activated. The equation for describing the ellipsoid shape is expressed in Eq. (7). The activation strategy is described in detail in Fig. 7. As shown in Fig. 7a, only the region filled with the slash lines is activated in one simulation time step during the single-track laser cladding process. This activation was because the region

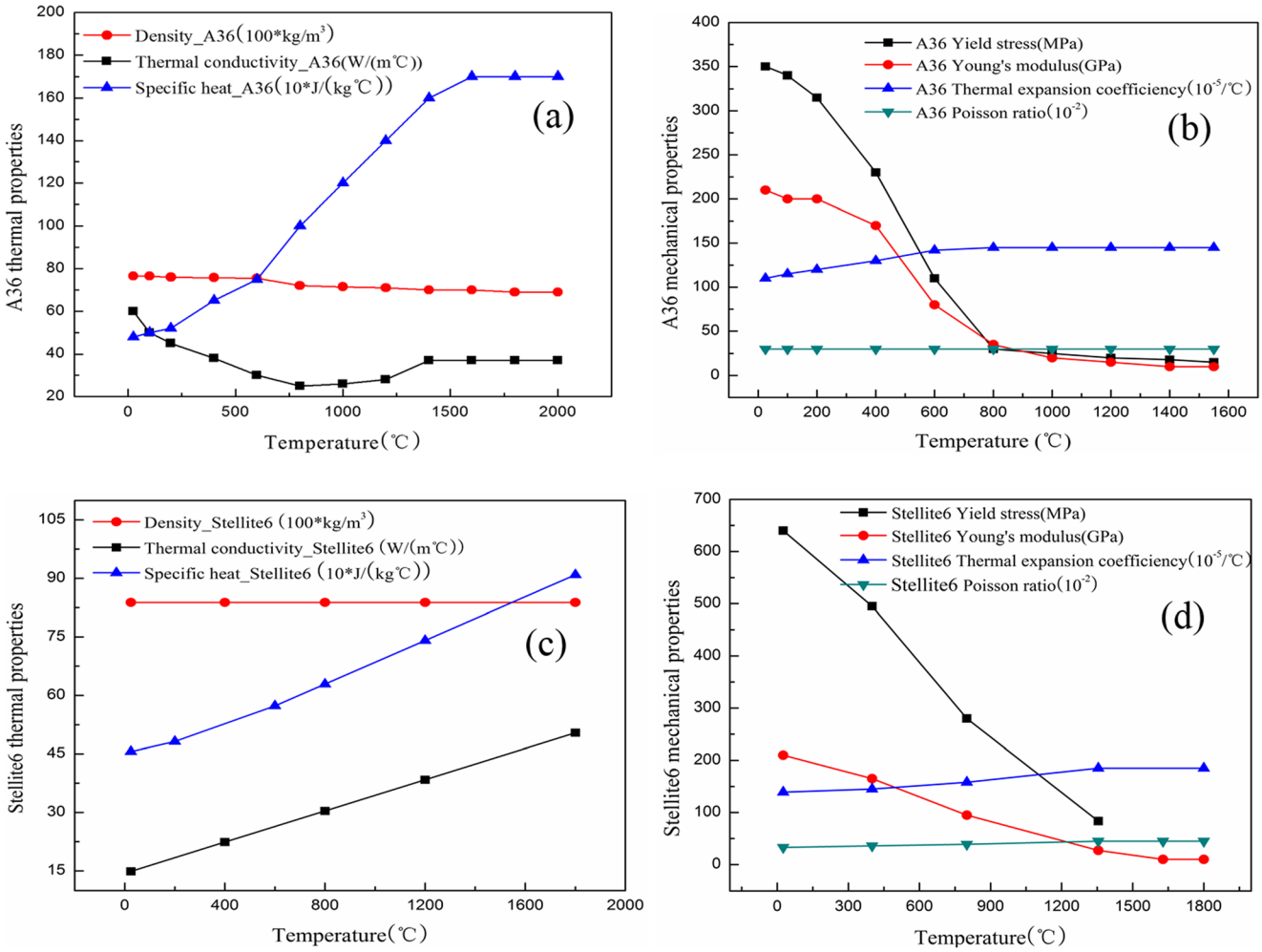

Fig. 5 Temperature dependent thermal properties, **a** thermal properties for A36, **b** mechanical properties for A36, **c** thermal properties for Stellite 6, and **d** mechanical properties for Stellite 6 [15, 24]

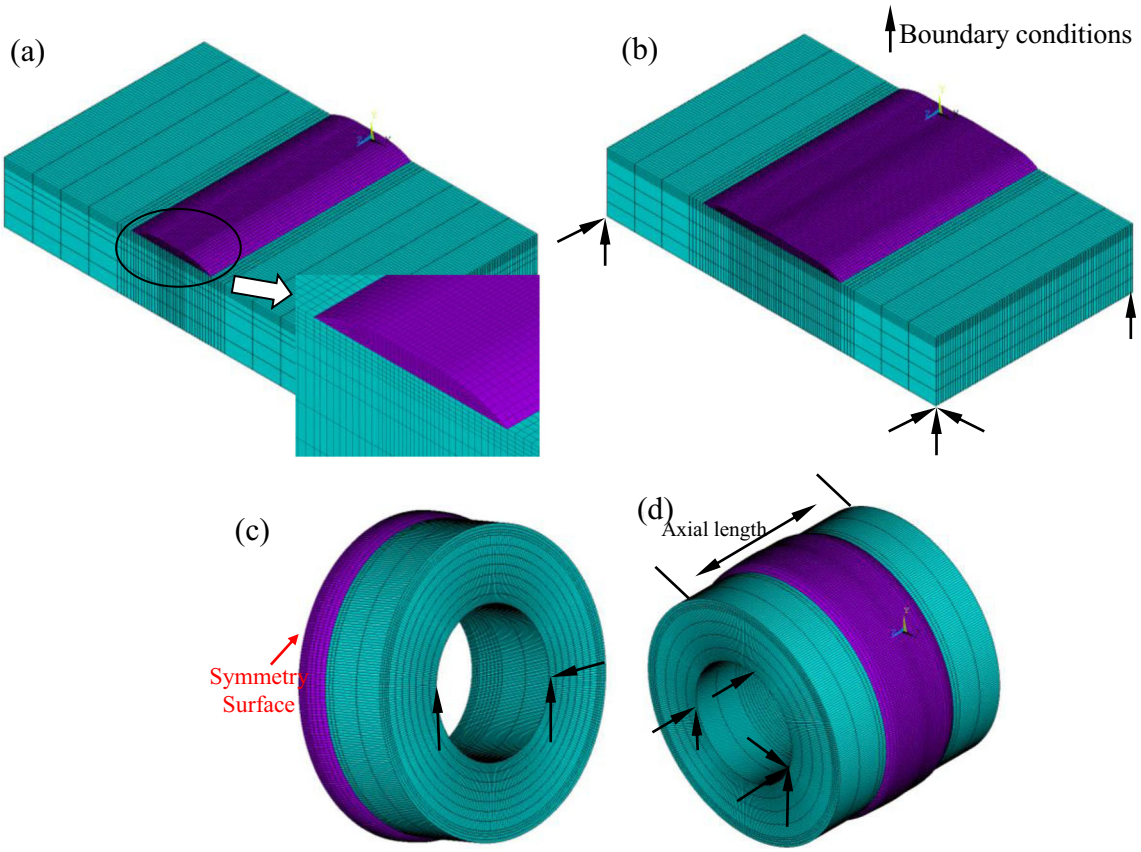

Fig. 6 Model geometry and mesh, **a** single-track flat model, **b** double-track flat model, **c** single-track cylindrical model, and **d** double-track cylindrical model

was not only irradiated by the laser heat source but the region was also below the ellipsoid surface. Figure 7b shows the activation strategy during the multi-track cladding process. During the deposition of the second track, elements were activated in the region that was below the ellipsoid surface, above the surface of the first track, and irradiated by the laser beam at the same time. The activated region in one simulation time step during the deposition of the second track is highlighted by the slash lines (see Fig. 7b).

$$\left(\frac{x}{b}\right)^2 + \left(\frac{y}{c}\right)^2 + \left(\frac{z}{a}\right)^2 = 1 \tag{7}$$

where b and c are the clad width and height respectively and are obtained from the experimental results. a

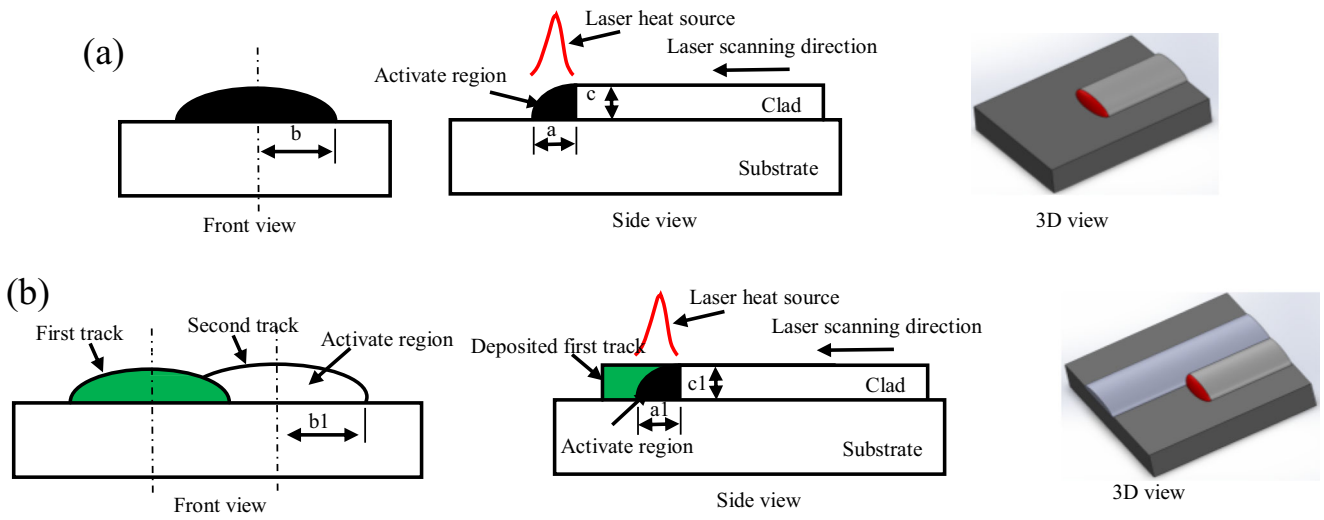

Fig. 7 The strategy for activating elements, **a** single track, **b** double track

represent the width of the laser beam and is equal to 3 mm in this study.

4.6 Solution

The commercial FE software ANSYS was applied to calculate the thermal and mechanical fields of the laser cladding process. In the current work, a sequenced thermo-mechanical simulation strategy was adopted. First, the thermal field of the laser cladding process was analyzed. The element type solid70 was selected for the thermal analysis. Then, the mechanical analysis was performed on the same mesh model. For the mechanical modeling, the element type was changed to solid 185. The temperature field obtained in the first step was input as thermal loadings. The mechanical boundary conditions were applied during calculation to avoid rigid body motion. The details of mechanical boundary conditions are represented by the arrows shown in Fig. 6. A flowchart is plotted in Fig. 8 that details the simulation procedure.

5 The validation of the simulation results

5.1 Thermal result validation

The accuracy of the simulated thermal results greatly influences the reliability of the calculated residual stress. Therefore, the simulated temperature distributions were first validated by the experiments. The cross-section contours of the single and double-track flat models obtained by experimentation and simulation are shown in Fig. 9. As Fig. 9a indicates, both the predicted cladding layer and the HAZ achieve a good correlation with the experimentation. Figure 9b shows the cross-section of the double-track flat model obtained experimentally. In the overlapping zone, the second track is deposited along the top surface of the first track (see Fig. 9b). Therefore, the laser heat flux should be applied perpendicularly to the surface of the first track in the overlapping zone during the simulation of the double-track flat model. The simulated cross-section temperature contour of the second track is shown in Fig. 9c. It can be concluded that the predicted results coincide very well with those obtained through experimentation.

Thermocouple measurements were applied to validate the simulated thermal history. Figure 10a illustrates the positons of the installed thermocouples for the single-track flat model. Figure 10b shows the numerically and experimentally obtained thermal histories for the single-track flat model. As Fig. 10b illustrates, the peak temperature of the T2 is higher than the T1. This result can be attributed to the heat accumulation during the laser cladding process. Figure 11 shows the thermal cycles of the two marked points obtained from the experiment and simulation of the double-track flat model. The positons of the monitored points are illustrated in Fig. 11a. Two peaks are presented for the double-track flat model because of the repeated heating of the laser beam. Through the comparison, it can be concluded that both the predicted peak temperatures and the cooling rates meet well with the measured data.

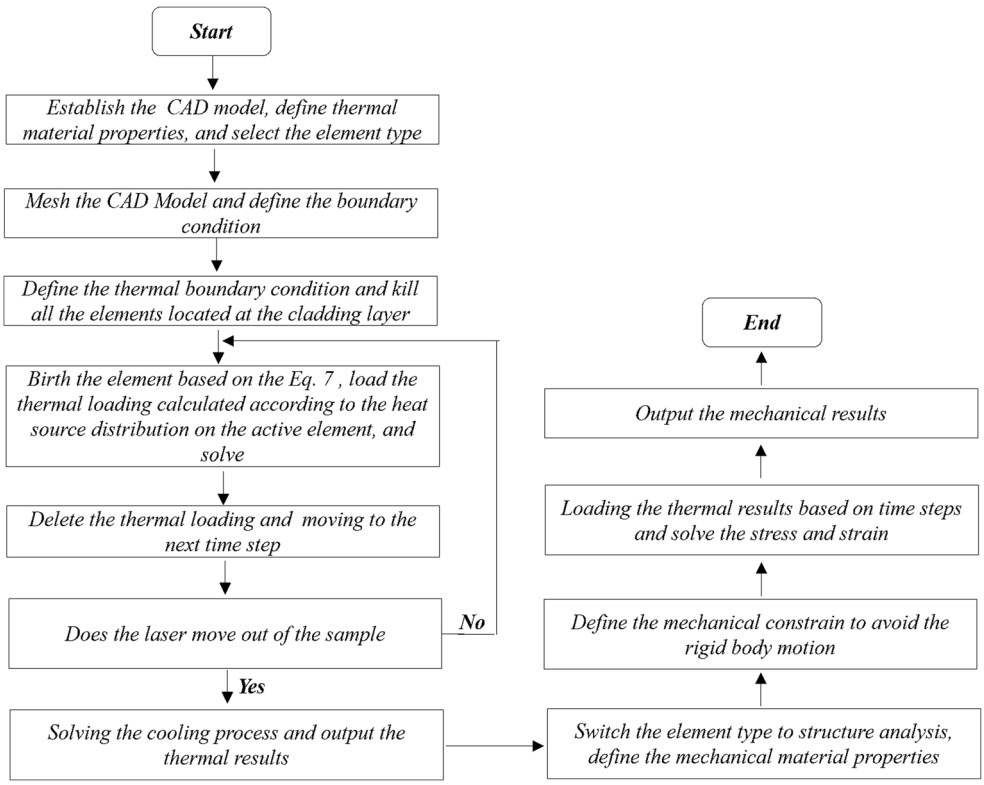

Fig. 8 The flowchart of simulation procedure

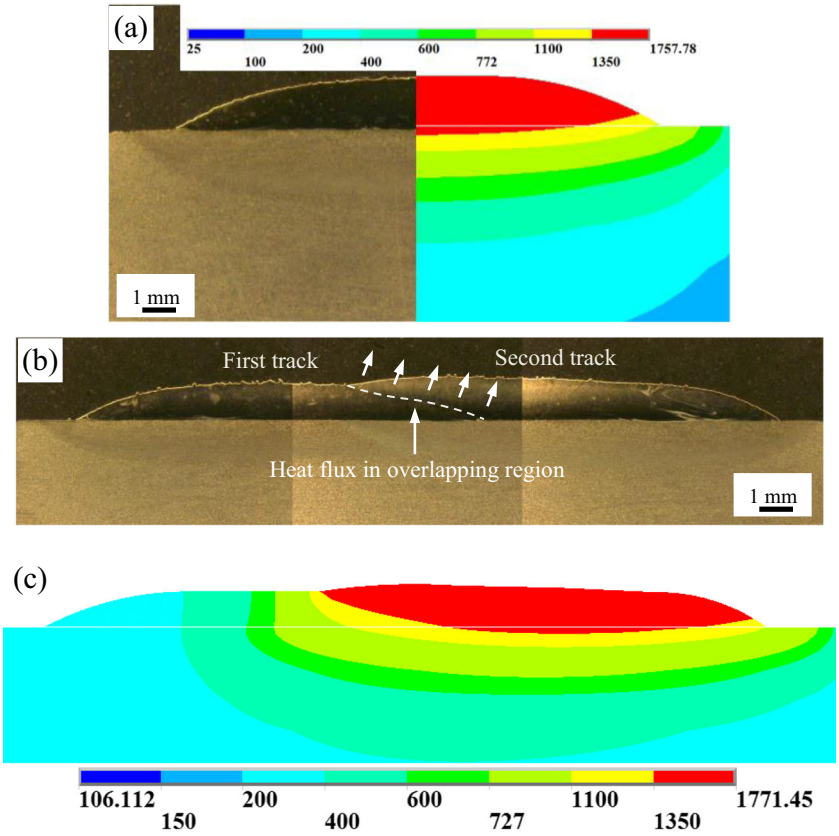

Fig. 9 Cross-section of clad, **a** experimental and prediction results of single-track flat model, **b** experimental result of double-track flat model, **c** prediction result of double-track flat model

Figure 12 illustrates the temperature contours of the flat model. The temperature contour of the first track is shown in Fig. 12a. The area of the red color represents the shape of the molten pool. The region near the molten pool was heated to a high temperature that dissipated to room temperature rapidly in the area away from the molten pool. This phenomenon indicated a sharp temperature gradient during the cladding. Figure 12b illustrates the temperature contour of the second track. The molten pool peak temperature of the second track was higher than that of the first track. This phenomenon can be explained by the heat accumulation in the substrate from the first track. Moreover, the clad in the overlapping zone of the first track was re-melted or reheated, which could result in the coarsening of the microstructure and decreasing of the mechanical properties.

5.2 Stress results validation

Figure 13 shows the comparison of the residual stress obtained by the experiment and simulation. The individual spots shown with error bar in Fig. 13 represent the experimental data

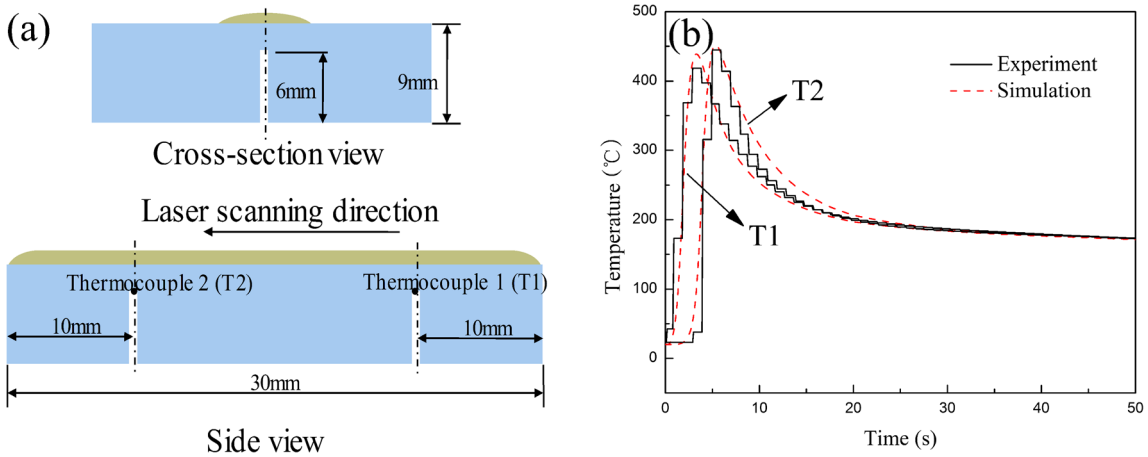

Fig. 10 Comparison between the predicted and experimental measurements for the single-track flat model, **a** positions of the thermocouples of T1 and T2, **b** thermal cycles of T1 and T2

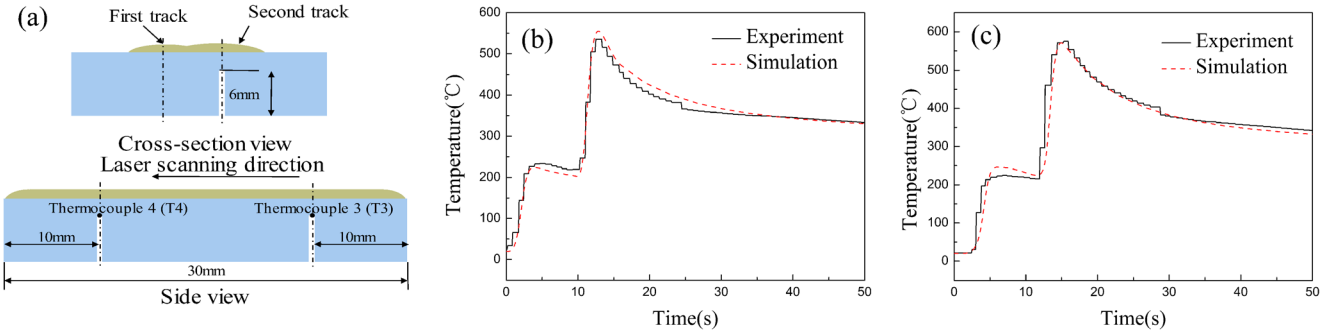

Fig. 11 Comparison between the predicted and experimental measurements for the double-track flat model, **a** positions of the thermocouples of T3 and T4, **b** thermal cycles of T3, c thermal cycles of T4

obtained using the XRD machine. The spots connected by the solid line represent data obtained from simulation. As Fig. 13 indicates, a qualitative agreement is achieved between the simulated residual stresses and measured values. The simulated results in the clad layer are higher than those obtained from the experiments. The differences between the prediction and measured results can be attributed to two reasons. First, the curved clad surface and un-melted powders as well as the XRD machine errors could lead to deviation during the measurement. Second, the stress-strain curve adopted in this study and the lack of high temperature material properties could decrease the prediction accuracy of the FE model.

6 Results and discussion

6.1 Flat model

Figure 14 shows the 3D residual stress contour of the single and double flat models. As Fig. 14a and b shows, both the longitudinal and transverse stresses in the cladding layer are tensile in nature. Compressive stress in the substrate at a distance away from the cladded layer was observed to balance the residual stress. The longitudinal and transverse residual stresses had a symmetry distribution according to the center of the clad. As the advancing direction of the cladding process, the longitudinal residual stress was higher than the transverse residual stress. Figure 14c and b plots the 3D contour of the residual stress distributions of the double-track flat model. The symmetry distribution pattern of the residual stress disappeared in the double-track flat model. The nature of the longitudinal and transverse residual stresses was still tensile in the cladded layer. Compressive transverse and longitudinal stresses were observed at the substrate's edges in order to equilibrate the tensile stress in the cladded layer. The highest longitudinal residual stress and transverse residual stress were both distributed at the overlapping region. The longitudinal residual stress in the first track of the double-track model was smaller compared to the single-track model. This stress relaxation can be attributed to the reheating of the first track during the cladding of the second track.

6.2 Cylindrical model

6.2.1 Effect of the axial length

The geometry dimensions of the established model influenced the stress distribution of the laser cladding process. The large size model increased the calculation time and made the model "expensive." The small size model resulted in a dimensional

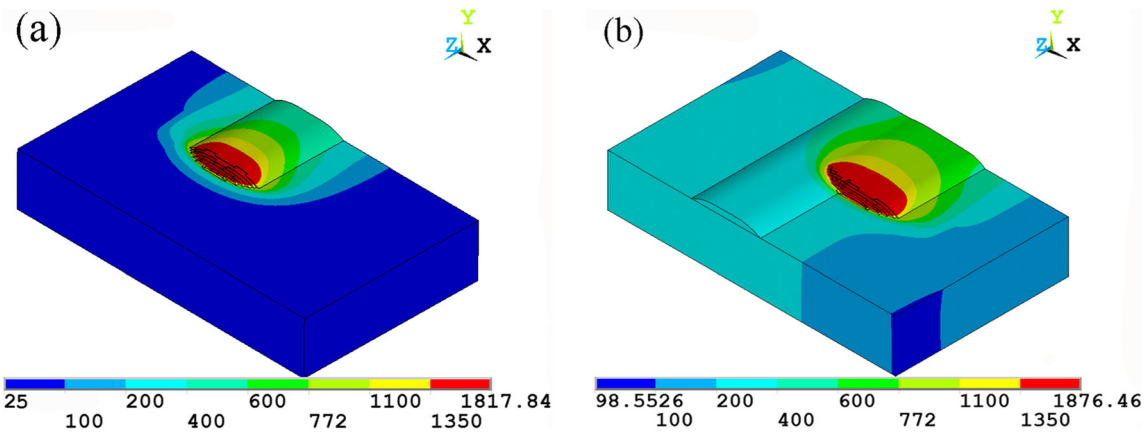

Fig. 12 The modeled temperature contours, **a** first track at 3 s, **b** second track at 12.7 s

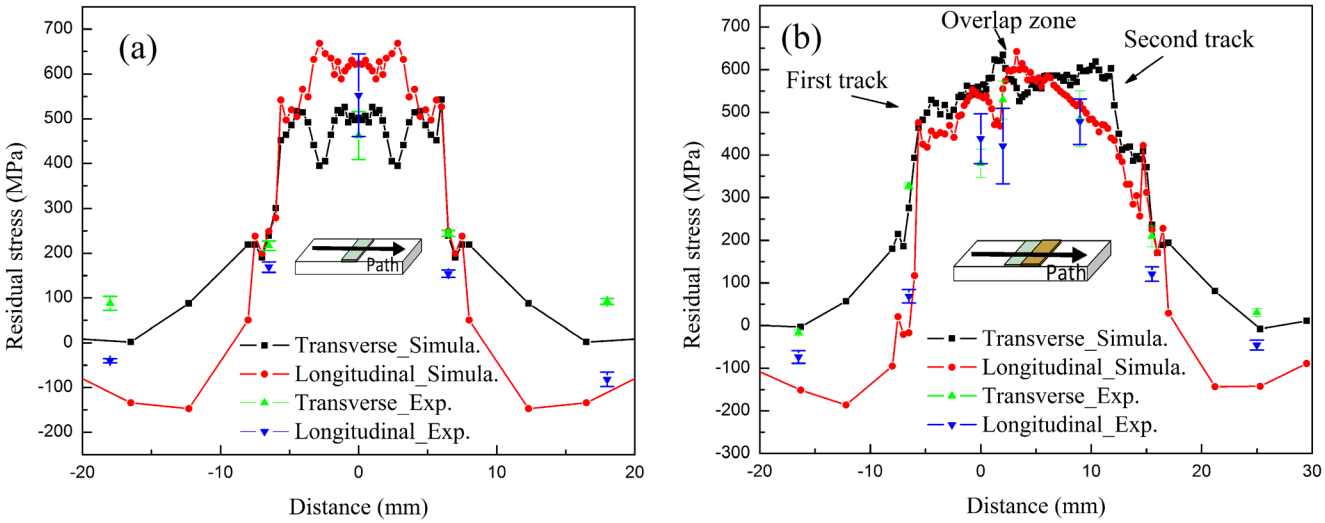

Fig. 13 Residual stress distributions of the flat model, **a** single track, **b** double track

effect and consequently influenced the accuracy of the simulation results. In this section, the effect of the axial length of the cylindrical model on the residual stress distribution was investigated. Figure 15 shows the residual stress distribution of the laser cladding single track on the cylindrical model. As Fig. 15a shows, the increase of the axial length from 50 to 200 mm does not change the hoop residual stress distribution. As shown for the axial stress, the cases under the axial length of 100 and 200 mm have exactly the same value and distribution. The axial stress at the cladding layer with the length of 50 mm was slightly higher than that of the cases with length of 100 and 200 mm. However, the difference was around 4%. As

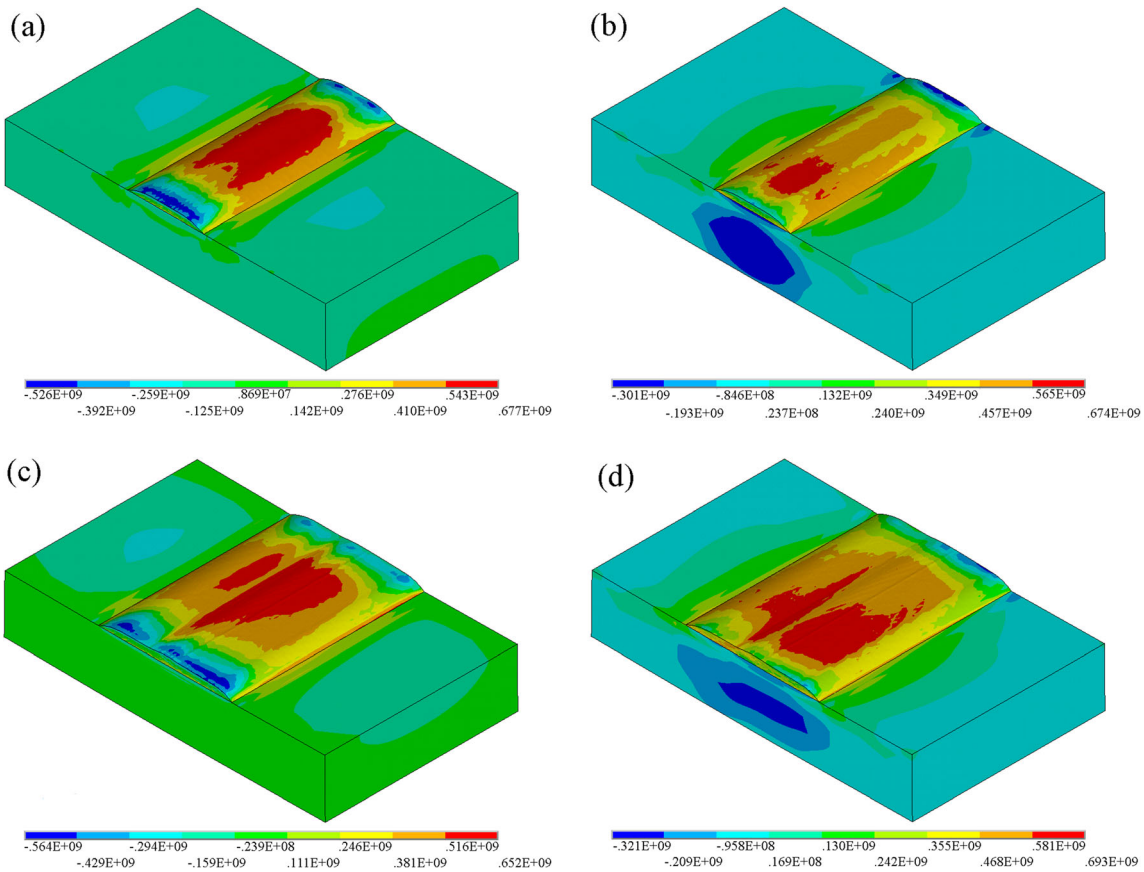

Fig. 14 3D contour of the residual stress distribution, **a** longitudinal direction of single-track flat model, **b** transverse direction of single-track flat model, **c** longitudinal direction of double-track flat model, and **d** transverse direction of double-track flat model

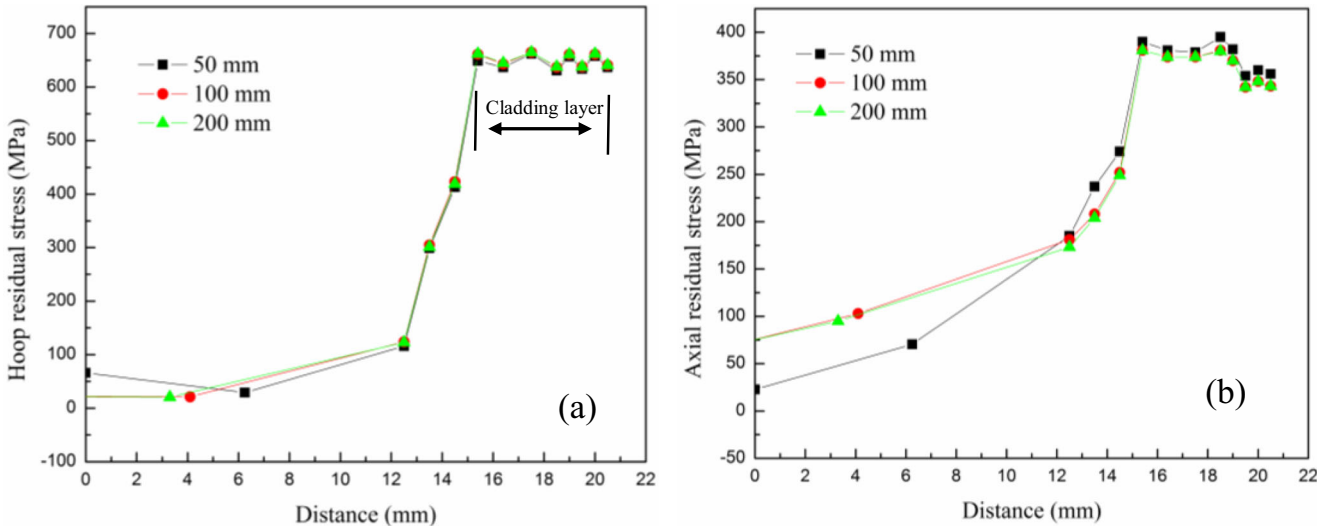

Fig. 15 The effect of the axial length on the residual stress distribution, **a** hoop stress, **b** axial stress

a result, by considering the calculation efficiency and the low difference of the simulation results (4%), 50 mm was selected as the axial length of the cylindrical model in this study.

6.2.2 The stress evolution

The stress evolution of three marked points in the double-track cylindrical model is shown in Fig. 16. P1 and P3 have compressive stress when they are heated by laser during cladding of the first track (see Fig. 16a). The stress for P2 was 0 due to the "death" of this point during the cladding of the first track. With the finish of the cladding of the first track, the stresses of P1 and P3 changed from a compressive to a tensile nature. This phenomenon could be attributed to the contraction of the cladded layer during the cooling procedure of the deposition of the first track. When the laser beam approached the marked points for the cladding of the second track, compressive stress was presented at the three marked points. When the cladding of the second track was finished, the model went into a cooling stage and the tensile stress was gradually induced at all marked points. P2 in the center of the first track and P3 in the overlapping region had higher hoop stress after the completion of the second track. The smallest hoop stress was presented at point P1 located at the center of the first track. Moreover, the value of the stress at point P1 during the cooling stage of the second track was lower than the value during the cooling of the first track. P1 was tempered during the cladding of the second track. This tempering resulted in stress relaxation and the subsequent decrease in tensile stress. As for the axial stress, points P1 and P3 had similar axial stress during the cooling stage of the first track. When the deposition of the second track finished, P1 in the first track and P3 in the overlap region had higher axial stress compared to that of P2 in the second track.

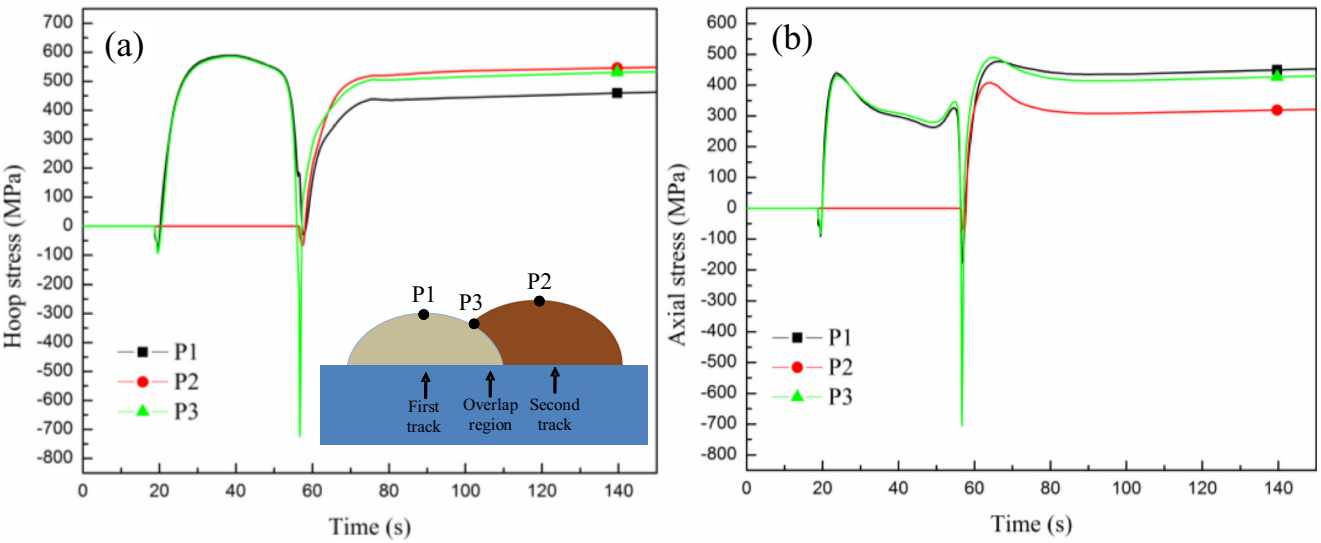

Fig. 16 Stress evolution versus time at different characteristic points at double-track cylindrical model, **a** hoop stress and **b** axial stress

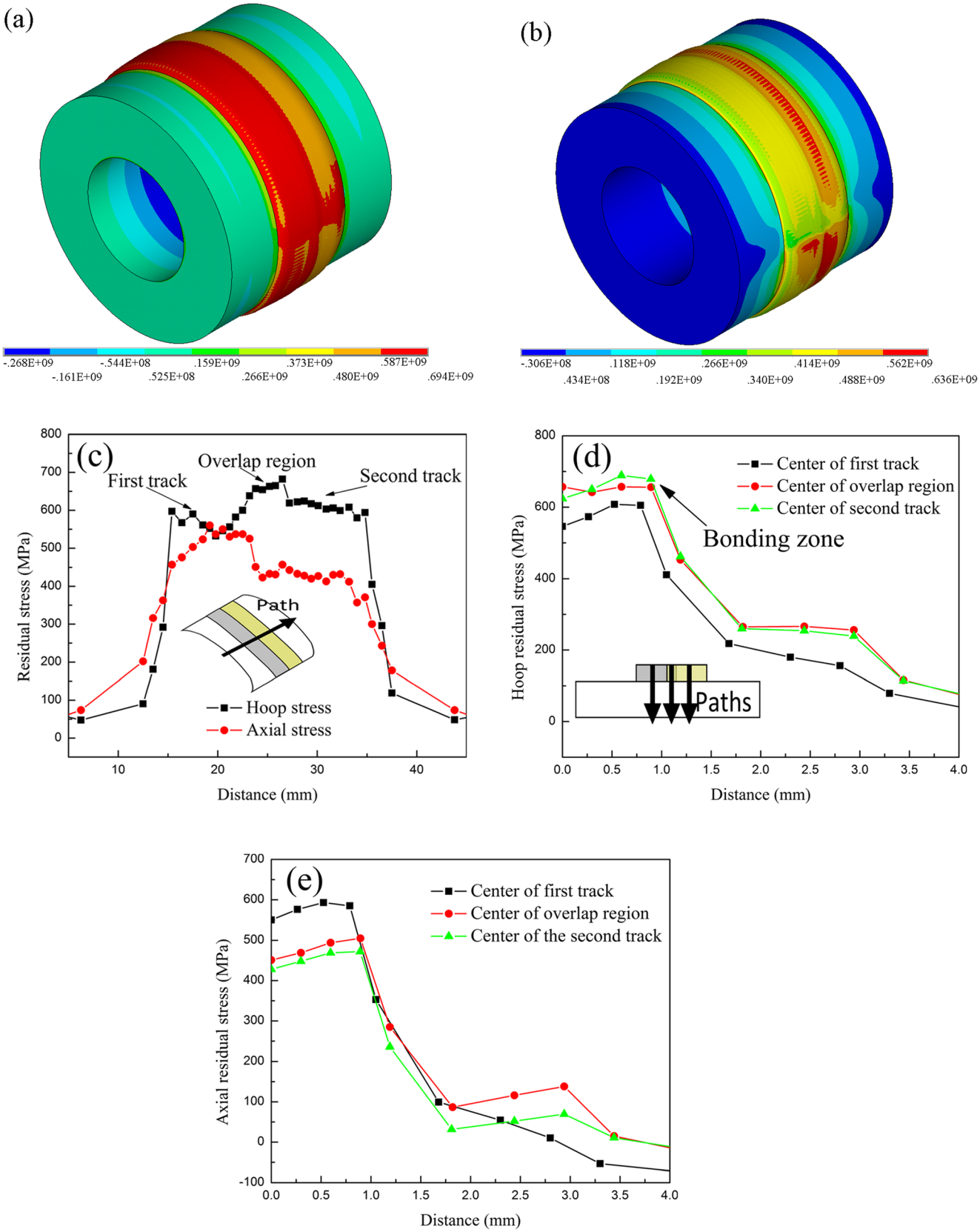

Fig. 17 Residual stress distributions of cylindrical double-track model, **a** 3D hoop residual stress, **b** 3D axial residual stress, **c** stress distribution on the top surface, **d** hoop stress distributed along the cross-section, **e** axial stress distributed along the cross-section

6.2.3 Residual stress distribution

The 3D view of the residual stress distribution for the double-track cylindrical model is given in Fig. 17a and b. As indicated from Fig. 17a, the hoop residual stress in the first track was lower than the second track due to the stress relaxation effect. It is interesting to mention that the axial residual stress in the first track was slightly higher than that in the second track. The detailed residual stress distributions on the upper surface of the cylindrical model are given in Fig. 17c. Both the magnitude hoop and axial residual stresses are presented in the overlapping region. Figure 17d and e shows the hoop and axial residual stress distributions in the radial (thickness) direction of the clad. The peak values of the hoop residual stress and axial residual stress were both distributed close to the interface between the clad and substrate. This phenomenon could be attributed to the high thermal gradient at the bonding zone as well as the mismatch of the material properties (especially the thermal expansion coefficient) between the clad layer and substrate [28, 29]. Similar to the residual stress distribution trend on the upper surface of the clad, the hoop residual stress in the overlapping region and second track along the radial direction was higher than the first track. In contrast, the axial residual stress in the center of the first track along the radial direction was higher than the other two paths.

6.2.4 Effect of preheating

The high stress generated during the laser cladding process could lead to cracks and finally resulted in the decrease of mechanical properties of the coating. Preheating is an effective method to mitigate the issue of cracks [30]. Preheating can decrease the temperature gradient and cooling rate during the cladding process. Therefore, the stress generated during the cladding process could be decreased and consequently resulted in achievement of a crack-free coating. In order to

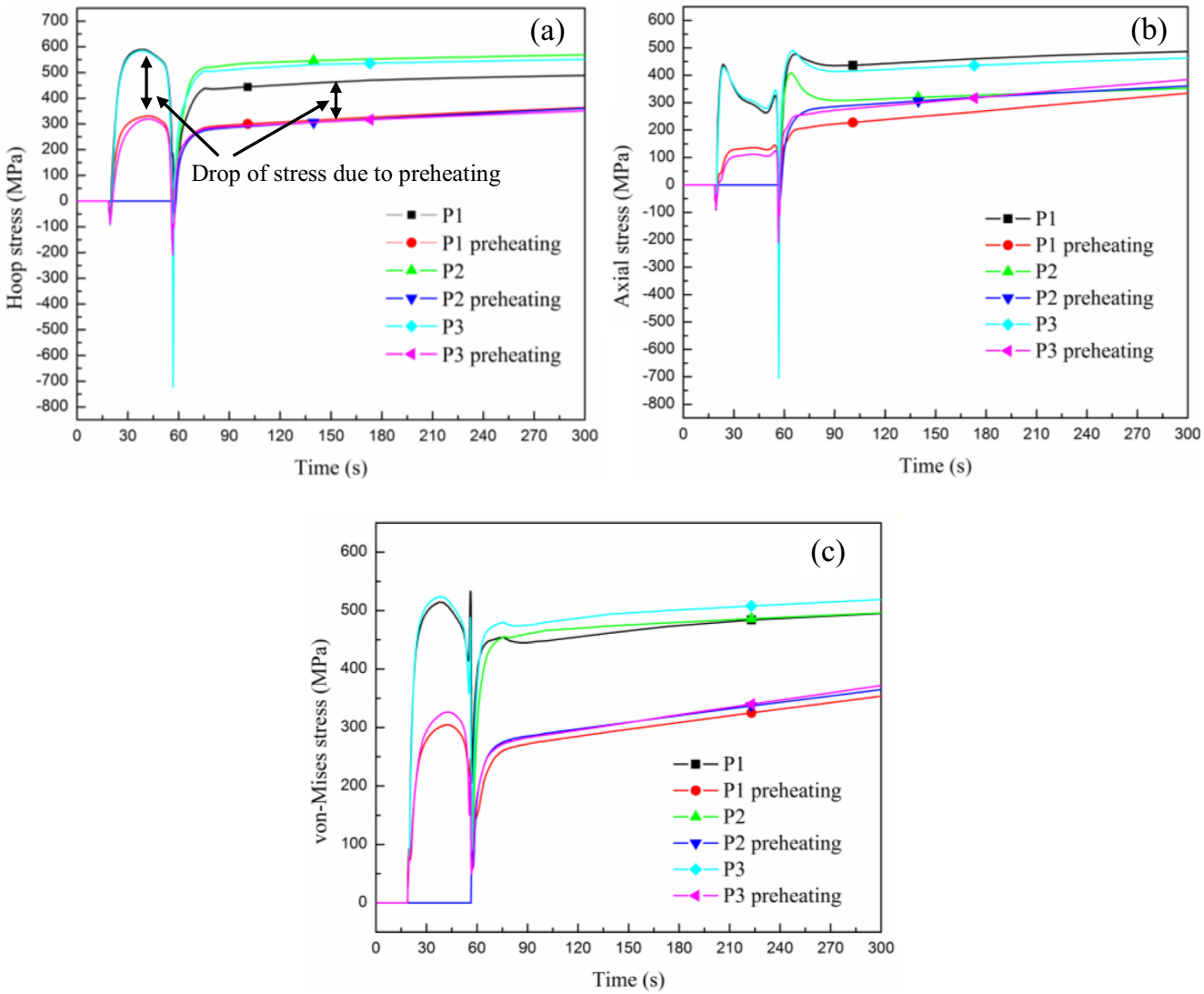

Fig. 18 Stress evolution of the marked points with and without preheating, **a** hoop stress, **b** axial stress, **c** von-Mises stress

investigate the effect of preheating on the stress distribution, a case of laser cladding double-track on cylindrical part with a preheating temperature of 550 °C was investigated. Figure 18 shows the stress evolution of the marked points with and without preheating. It can be inferred from Fig. 18 that the hoop stress, axial stress, and von-Mises stress for the three marked points are all decreased after preheating. A magnitude drop of 200 MPa of the von-Mises stress after the preheating is observed (see Fig. 18c). The material at high temperature generally has low strength. The existence of tensile stress at high temperature increased the hot cracking susceptibility of the coating during the cladding process [31]. By preheating, the stress magnitude dropped greatly just after the cladding process, and consequently, lowered the cracking tendency. Figure 19 shows the distribution of the residual stress on the top surface of the clad for cases with and without preheating. As Fig. 19 indicates, the hoop residual stress is decreased with the help of preheating. The axial residual stress in the second track was increased slightly after preheating. The distribution of the von-Mises residual stress shows that the preheating does have a positive effect on the decrease of residual stress (see Fig. 19c). However, the decrease of amplitude of the residual stress value was limited. In conclusion, preheating could greatly decrease the stress magnitude during and just after the cladding process. The hoop and von-Mises residual stresses were decreased by heating. Preheating did not have an obvious effect on the axial residual stress.

Figure 20a shows the dye penetration test result for the clad without preheating. As the figure indicates, many cracks are shown on the clad surface. Most of these cracks originated and propagated from the overlapping region (see Fig. 20a and c). Figure 20d shows that a crack originates from the clad-substrate interface and propagates to the surface of the clad. A similar crack initiation and propagation pattern was also

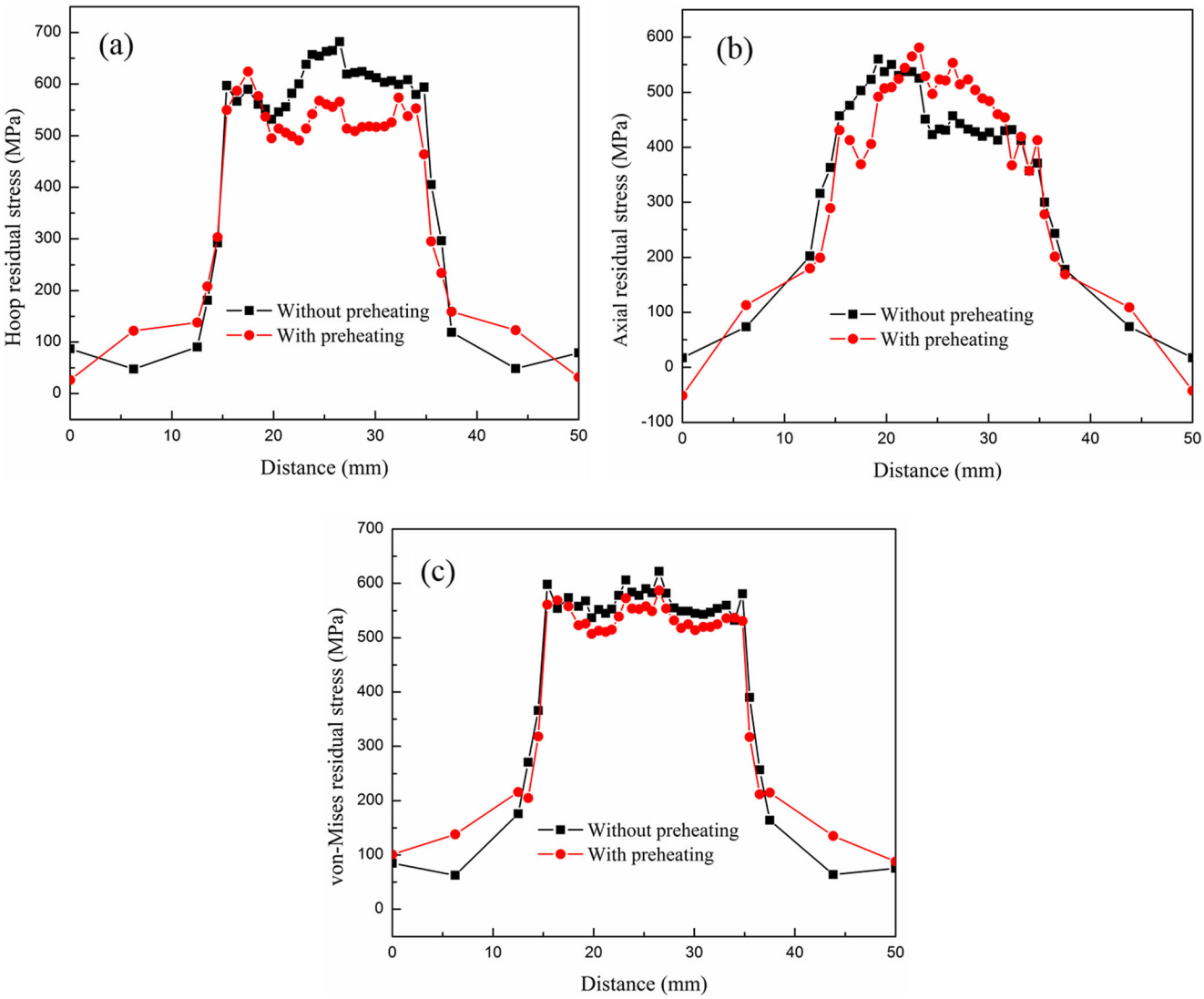

Fig. 19 Residual stress distribution on the top surface of clad for the double-track cylindrical model, **a** hoop residual stress, **b** axial residual stress, **c** von-Mises stress

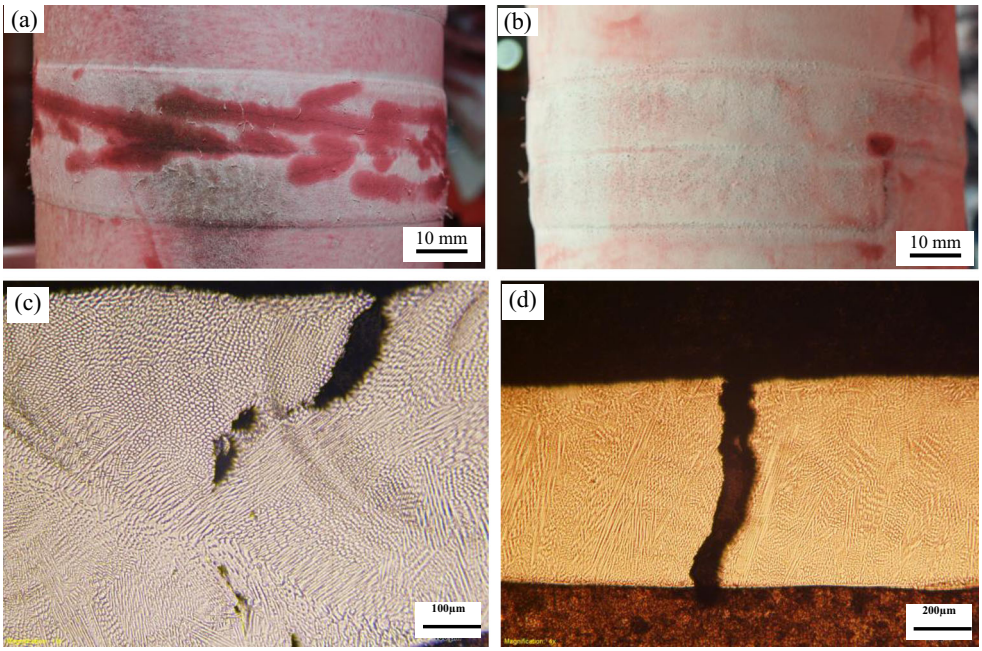

Fig. 20 Laser cladding of double-track on cylindrical part, **a** dye penetration test without preheating, **b** dye penetration test with preheating 550 °C, **c** crack at overlap region, **d** crack across the clad cross-section

reported by Wang et al. [32]. According to our simulation results, high tensile hoop and axial stresses were obtained at the overlapping region and the clad interface, which resulted in the crack's initiation and propagation at these regions. Figure 20b shows the dye penetration test results of the coupon with a preheating temperature of 550 °C. The cracks were eliminated completely by introducing the preheating, which demonstrated the positive effect of preheating on the mitigation of cracks during the laser cladding process. This experimental observation met very well with our simulation results. Our simulation results showed a great decrease of the stress magnitude just after the cladding process through preheating (see Fig. 18). This drop of the stress magnitude greatly decreased the crack susceptibility during the cladding process.

7 Conclusions

In this study, the stress evolution of the laser cladding of cobalt-based alloys was investigated using the FE method. The stress distributions in three different cases, the single-track flat model, double-track flat model, and double-track cylindrical model, were discussed in detail. Based on the presented study, a few points can be described as follows:

(1) In the single-track flat model, the cladding layer had tensile residual stress both in the transverse and longitudinal directions. In the double-track flat model, high residual stress was observed at the second track and overlapping region. The residual stress in the first track was relieved due to the reheating effect of the second track.

(2) In the cylindrical double-track model, the hoop residual stress in the second track was higher than the first track. The axial residual stress in the second track was slightly lower than the first track. Similar to the double-track flat model, the clad-substrate interface and overlapping region had high tensile stress that increased the crack susceptibility in these two regions.

(3) For the double-track cylindrical case, cracks initiated from the overlapping region and clad-substrate interface. Preheating greatly decreased the stress just after the cladding process and consequently reduced the crack susceptibility of the coating. Preheating had insignificant effect on the decrease of the residual stress for the double-track cylindrical model.

Acknowledgements The authors would like to thank Andrew Socha, a research engineer at the Research Center for Advanced Manufacturing, for his help in the execution of experiments. The first author, Zhe Zhang, would like to thank Dr. Lin Zhu, a former Ph.D. candidate at the Department of Mechanical Engineering, Southern Methodist University, for his support and encouragement during the preparation of this work.

Funding information This work was financially supported by the NSF's Grant No. IIP-1539853.

References

1. Zhong M, Liu W (2010) Laser surface cladding: the state of the art and challenges. Proc Inst Mech Eng, Part C 224:1041–1060

2. Zhang Z, Yu T, Kovacevic R (2017) Erosion and corrosion resistance of laser cladded AISI 420 stainless steel reinforced with VC. Appl Surf Sci 410:225–240
3. Song L, Zeng G, Xiao H, Xiao X, Li S (2016) Repair of 304 stainless steel by laser cladding with 316L stainless steel powders followed by laser surface alloying with WC powders. J Manuf Process 24:116–124
4. Wang X, Chou K (2017) Electron backscatter diffraction analysis of Inconel 718 parts fabricated by selective laser melting additive manufacturing. JOM 69:402–408
5. Zhang Z, Kovacevic R (2016) Multiresponse optimization of laser cladding steel+ VC using grey relational analysis in Taguchi Method. JOM 68:1762–1773
6. Yang G, Liu Z, Wang Y (2013) Influence of molybdenum on the microstructure and mechanical properties of TiC-TiB2 reinforced metal matrix composite coatings. Sci China Technol Sc 56:1008–1016
7. Wang X, Keya T, Chou K (2016) Build height effect on the Inconel 718 parts fabricated by selective laser melting. Proc Manuf 5:1006–1017
8. Weng F, Chen C, Yu H (2014) Research status of laser cladding on titanium and its alloys: a review. Mater Des 58:412–425
9. Luo KY, Jing X, Sheng J, Sun GF, Yan Z, Lu JZ (2016) Characterization and analyses on micro-hardness, residual stress and microstructure in laser cladding coating of 316L stainless steel subjected to massive LSP treatment. J Alloy Compd 673:158–169
10. X. Wang, K. Chou, A method to estimate residual stress in metal parts made by Selective Laser Melting. Proc. ASME 2015 Int. Mech. Eng. Congr. Expo. Am. Soc. Mech. Eng. 2015, p. V02AT02A002
11. Yan Z, Liu W, Tang Z, Liu X, Zhang N, Li M, Zhang H (2018) Review on thermal analysis in laser-based additive manufacturing. Opt Laser Technol 106:427–441
12. Nazemi N, Urbanic RJ (2018) A numerical investigation for alternative toolpath deposition solutions for surface cladding of stainless steel P420 powder on AISI 1018 steel substrate. Int J Adv Manuf Tech 96:4123–4143
13. Heigel JC, Michaleris P, Reutzel EW (2015) Thermo-mechanical model development and validation of directed energy deposition additive manufacturing of Ti–6Al–4V. Addit. Manuf. 5:9–19
14. Jendrzejewski R, Śliwiński G, Krawczuk M, Ostachowicz W (2004) Temperature and stress fields induced during laser cladding. Comput Struct 82:653–658
15. Suarez A, Amado JM, Tobar MJ, Yáñez A, Fraga E, Peel MJ (2010) Study of residual stresses generated inside laser cladded plates using FEM and diffraction of synchrotron radiation. Surf. Coat. Tech. 204:1983–1988
16. P. Farahmand, R. Kovacevic, R, An experimental–numerical investigation of heat distribution and stress field in single-and multi-track laser cladding by a high-power direct diode laser, Opt Laser Technol 63 (2014) 154–168
17. Chew Y, Pang JHL, Bi G, Song B (2015) Thermo-mechanical model for simulating laser cladding induced residual stresses with single and multiple clad beads. J. Mater. Process Tech. 224:89–101
18. Bailey NS, Katinas C, Shin YC (2017) Laser direct deposition of AISI H13 tool steel powder with numerical modeling of solid phase transformation, hardness, and residual stresses. J. Mater. Process Tech. 247:223–233
19. Jeshvaghani RA, Shamanian M, Jaberzadeh M (2011) Enhancement of wear resistance of ductile iron surface alloyed by stellite 6. Mater Des 32:2028–2033
20. Singh R, Kumar D, Mishra SK, Tiwari SK (2014) Laser cladding of Stellite 6 on stainless steel to enhance solid particle erosion and cavitation resistance. Surf. Coat. Tech. 251:87–97
21. Zhang Z, Farahmand P, Kovacevic R (2016) Laser cladding of 420 stainless steel with molybdenum on mild steel A36 by a high power direct diode laser. Mater Des 109:686–699
22. Mohammadpour M, Yazdian N, Yang G, Wang H P, Carlson B, Kovacevic R (2018). Effect of dual laser beam on dissimilar welding-brazing of aluminum to galvanized steel. Opt Laser Technol 98: 214–228
23. Liu J, Wang Y, Li H, Costil S, Bolot R (2017) Numerical and experimental analysis of thermal and mechanical behavior of NiCrBSi coatings during the plasma spray process. J. Mater. Process Tech. 249:471–478
24. Nadimi S, Khoushehmehr RJ, Rohani B, Mostafapour A (2008) Investigation and analysis of weld induced residual stresses in two dissimilar pipes by finite element modeling. J Appl Sci 8:1014–1020
25. Zhang J, Liou F, Seufzer W, Taminger K (2016) A coupled finite element cellular automaton model to predict thermal history and grain morphology of Ti-6Al-4V during direct metal deposition (DMD). Addit Manuf 11:32–39
26. Hofman JT, De Lange DF, Pathiraj B, Meijer J (2011) FEM modeling and experimental verification for dilution control in laser cladding. J Mater Process Tech 211:187–196
27. Knapp GL, Mukherjee T, Zuback JS, Wei HL, Palmer TA, De A, DebRoy T (2017) Building blocks for a digital twin of additive manufacturing. Acta Mater 135:390–399
28. Zhang CS, Li L, Deceuster A (2011) Thermomechanical analysis of multi-bead pulsed laser powder deposition of a nickel-based superalloy. J Mater Process Technol 211:1478–1487
29. Wang F, Mao H, Zhang D, Zhao X, Shen Y (2008) Online study of cracks during laser cladding process based on acoustic emission technique and finite element analysis. Appl Surf Sci 255:3267–3275
30. Farahmand P, Liu S, Zhang Z, Kovacevic R (2014) Laser cladding assisted by induction heating of Ni–WC composite enhanced by nano-WC and La2O3. Ceram Int 40 (15421–15438
31. Fallah V, Alimardani M, Corbin SF, Khajepour A (2010) Impact of localized surface preheating on the microstructure and crack formation in laser direct deposition of Stellite 1 on AISI 4340 steel. Appl Surf Sci 257:1716–1723
32. Wang D, Hu Q, Zeng X (2015) Residual stress and cracking behaviors of Cr13Ni5Si2 based composite coatings prepared by laser-induction hybrid cladding. Surf Coat Tech 274:51–59